PAPER

Standing carbon-coated molybdenum dioxide nanosheets on graphene: morphology evolution and lithium ion storage properties†

Lei Guo and Yong Wang*

Transitional metal oxides are a class of high-capacity anodes for lithium ion batteries. Drastic volume changes during cycling and intrinsically poor electronic conductivity diminish their electrochemical performances such as cycliability and high-rate capabilities. This study reports an unprecedented MoO_2/ carbon network, consisting of the standing carbon-coated MoO_2 nanosheets on graphene nanosheets to solve these problems. The obtained MoO_2 products can be tuned to have particle-like, rod-like, or sheet-like morphologies (standing MoO_2@C core–shell nanosheets or flat-lying MoO_2 nanosheets) on graphene by adjusting the experimental parameters. Due to the unique three dimensional porous MoO_2@C/graphene hierarchical structure, the composite manifests excellent electrochemical properties including high capacity, long cycle life and stable high-rate performances. A large reversible capacity of above 500 mA h g^{-1} can be achieved after 200 cycles at a large current of 5 A g^{-1}.

Introduction

Rechargeable lithium-ion batteries (LIBs), as popular electrochemical energy storage system, have been applied in the fields of portable electronic devices, hybrid electrical vehicles, and electrical vehicles. The development of electrode materials with satisfactory properties, in terms of high capacity, long cycle life and good rate capability, have been the hot topic for next-generation LIBs.[1–3] Graphite, used as conventional anode material, has a limited theoretical specific capacity of 372 mA h g^{-1}. Transition metal oxides have attracted significant research concerns due to their higher gravimetric and volumetric capacity. For example, MoO_2 possesses a high theoretical capacity of 838 mA h g^{-1}, which has been proposed as a potential anode candidate for lithium-ion batteries.[4–7] However, the drastic volume change of MoO_2 and other transitional metal oxides during cycling gives rise to electrode pulverization and subsequently fast capacity decay.

Nanostructured electrodes have been demonstrated to deliver better electrochemical performances than their bulky counterparts due to the shortened electronic and ionic diffusion pathway, larger active surface area, and enhanced reaction kinetics.[8–19] Hybridizing metal oxides with carbon materials

(such as carbon coating[20–28] and carbon support[29–42]) is also an effective strategy to buffer the critical problem of volume change. Graphene, owing to its unique properties, such as ultrahigh surface area, excellent thermal and electronic conductivity, and highly flexible and robust structure, has been demonstrated as a good support for the preparation of various graphene-based high-capacity composites.[33–40,43–48] MoO_2 nanostructures with diverse morphologies, including nanoparticle,[8,9] nanosheet,[10] nanorod,[11–13] nanotube,[14,15] mesoporous structure,[16,17] and core–shell structure,[18,19] have been synthesized and explored as anodes for Li-ion batteries. Moreover, MoO_2/carbon nanocomposites, such as carbon-coated MoO_2,[20–28] MoO_2/mesoporous carbon,[29,30] MoO_2/carbon nanotube,[31,32] and MoO_2/graphene,[33–40] with enhanced electrochemical performances have been reported recently. It is worth noting that MoO_2 has been fabricated with nanoparticle morphology in most MoO_2/graphene reports,[33–40] whereas MoO_2 fabricated with nanorods morphology obtained on graphene is found in a single report.[37] Graphene supported MoO_2 nanoparticles can be also self-assembled into a rod-like nanostructure.[40]

In this study, we developed a facile one-step thermolysis method for fabricating two-dimensional graphene support of four types of MoO_2 morphologies and explore their morphology-dependent lithium-storage applications. The standing MoO_2@C nanosheet or flat-lying MoO_2 nanosheet on graphene, MoO_2/graphene rod-on-sheet and particle-on-sheet composites can be obtained by varying the experimental conditions. Such a unique hierarchical graphene-based structure, namely the standing or flat-lying MoO_2 nanosheets on graphene, has not been witnessed previously. The three dimensional porous structure of carbon-coated MoO_2 nanosheets erected on

Department of Chemical Engineering, School of Environmental and Chemical Engineering, Shanghai University, Shangda Road 99, Shanghai, P. R. China, 200444. E-mail: yongwang@shu.edu.cn; Fax: +86-21-66137725; Tel: +86-21-66137723

† Electronic supplementary information (ESI) available: Elemental mapping, SEM, TEM, XRD and electrochemical performance of MoO_2 based composites. See DOI: 10.1039/c4ta05520a

graphene is found to be a more suitable morphology as an anode for Li-ion batteries. It delivers a large capacity of 752 mA h g^{-1} after 100 cycles at a small current of 100 mA g^{-1} and remains a large capacity of 502 mA h g^{-1} after 200 cycles at an extremely large current of 5 A g^{-1}.

Experimental section

Materials synthesis

All chemicals were used as received without further purification. Graphene nanosheets (GNS) were prepared by a modified Hummers method, followed by a thermal reduction as reported previously.[44,48] For the typical synthesis of MoO$_2$@C nanosheet/ graphene sheet-on-sheet composite, GNS (0.036 g) and hexaammonium heptamolybdate (AHM, 0.05 g) tetrahydrate were dissolved in ethanol (20 mL) and then ultrasonicated for 30 min. The solid precursor was obtained by evaporating the ethanol solvent at 80 °C for 12 h and subsequently treating in a tube furnace at 550 °C for 2 h under flowing 40 sccm gas mixtures of 5% C$_2$H$_2$ and 95% N$_2$. To explore the effect of graphene in the composite, various amounts of GNS were also used for the preparation of MoO$_2$@C/graphene sheet-on-sheet composites with different loadings of MoO$_2$.

MoO$_2$/graphene sheet-on-sheet and particle-on-sheet composites were prepared in a similar preparation process by replacing 5% C$_2$H$_2$/N$_2$ with pure N$_2$ or 5% H$_2$/N$_2$. A mixture of MoO$_2$/graphene rod-on-sheet and particle-on-sheet structures was prepared in 5% C$_2$H$_2$/N$_2$ by replacing AHM with phosphomolybdic acid (PMA) hydrate. MoO$_2$@C product was prepared by a similar method in the absence of GNS.

Materials characterization

The obtained products were characterized by X-ray diffraction (XRD, Rigaku D/max-2550V, Cu Kα radiation), field-emission scanning electron microscopy (FE-SEM, JSM-6700F) with an energy dispersive X-ray spectrometer (EDS), transmission electron microscopy and high-resolution transmission electron microscopy (TEM, HRTEM, JEOL JEM-200CX and JEOL 2010F). Raman spectroscopy was recorded on a Renishaw in plus laser Raman spectrometer (excitation wavelength: 785 nm, excitation power: 3 mW, spot size: ~1.2 μm). The Brunauer–Emmett–Teller (BET) surface area and porous structures were measured by an accelerated surface area and porosimetry analyzer (Micromeritics Instrument Corp, ASAP 2020 M + C, analysis adsorptive: N$_2$). Thermogravimetric analysis (TGA) was performed on a NETZSCH STA 409 PG/PC instrument under air atmosphere at a ramp rate of 10 °C min^{-1}.

Electrochemical measurements

The Swagelok-type cells were assembled in an argon-filled glovebox and used to measure the electrochemical performances. The working electrodes were composed of active material, acetylene black and poly (vinylidene difluoride) (PVDF) at a weight ratio of 80 : 10 : 10 in N-methyl pyrrolidinone (NMP). The loading amount of the electrode on copper foil was kept at ~2 mg cm^{-2} and the thickness was ~20 micrometers. The

specific capacity was calculated based on the total weight of the composite electrode materials. Lithium foil was used as the reference electrode. The electrolyte was 1 M LiPF$_6$ dissolved in a mixture of ethylene carbonate (EC) and diethyl carbonate (DEC) (1 : 1 w/w). The cells were discharged (lithium insertion) and charged (lithium extraction) at a constant current (100 mA g^{-1}, 0.1 C, 1 C = 1000 mA g^{-1}) in the fixed voltage range from 5 mV to 3.0 V. Higher hourly rates (1, 5, or 10 C) were also used, and the first cycle discharging was kept at 0.1 C. Cyclic voltammetry (CV) was performed on a CHI660D electrochemical workstation at a scan rate of 0.1 mV s^{-1}. Nyquist plots were collected on the same workstation for various electrodes from 100 kHz to 0.01 Hz.

Results and discussion

Scheme 1 illustrates the growth process of four distinct morphologies of MoO$_2$/graphene composites, which was obtained using a one-step facile thermolysis technique. MoO$_2$ particles were obtained on graphene in 5% H$_2$/N$_2$, while MoO$_2$ nanosheets were observed on graphene in pure N$_2$ gas. If C$_2$H$_2$ was used, carbon-coated MoO$_2$ (MoO$_2$@C) nanosheets were formed and erected on GNS. After stacking, these standing MoO$_2$ nanosheets on graphene would form a three dimensional porous MoO$_2$/graphene layer-by-layer nanostructure, in which there is void space among standing MoO$_2$ nanosheets to accommodate the volume expansion and facilitate the charge transfer. On the other hand, the graphene nanosheets were efficiently separated with large distance by these standing MoO$_2$ nanosheets. Amorphous carbon coating from C$_2$H$_2$ decomposition was used as a binder to link MoO$_2$ and graphene and make the composite structure stable. The abovementioned three composites are all prepared using hexaammonium heptamolybdate (AHM) tetrahydrate as the precursor source of MoO$_2$. When another precursor of phosphomolybdic acid
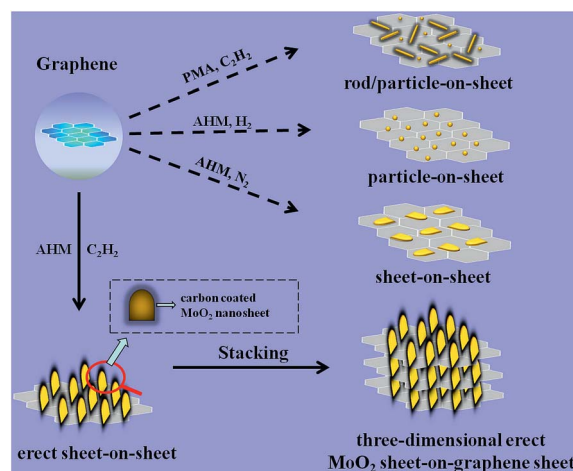
Scheme 1 Schematic illustration showing the synthesis process of the graphene supported MoO$_2$ of various morphologies. The structure of standing carbon-coated MoO$_2$ (MoO$_2$@C) nanosheets on graphene is the main product of this study, which forms a sandwiched 3D porous network after stacking.

(PMA) hydrate was used under flowing C_2H_2, carbon coated MoO_2 with a mixture morphology of nanorods and nanoparticles were obtained as the final product on graphene.

Fig. 1 shows SEM images of graphene nanosheets (GNS), MoO_2@C particles and the standing MoO_2@C nanosheets on graphene. Graphene is wrinkled and very thin under electron imaging (Fig. 1a). MoO_2@C is prepared by the decomposition of AHM under flowing acetylene gas in the absence of graphene. Particles with irregular shape are observed and their surface is rather smooth, indicating a carbon overlayer may be present (Fig. 1b). The carbon layer can be confirmed by the corresponding EDS spectrum in Fig. 1c and elemental mapping images (Fig. S1, ESI†). A uniform distribution of a pyrolytic carbon layer from the decomposition of acetylene is present in the MoO_2@C composite. Fig. 1d and e shows SEM images of graphene supported MoO_2@C nanosheets. Interestingly, a large number of small nanosheets were wrapped by graphene nanosheets and most nanosheets are found to stand on the graphene surface. These observed MoO_2 nanosheets interweave with graphene nanosheets, forming a sandwiched three dimensional porous network after stacking. Because MoO_2 nanosheets are erect rather than flat-lying on GNS, more open and porous spaces are introduced into the network of the packed MoO_2/graphene composite electrode. This will facilitate the diffusion of lithium ions and electrons and electrolyte infusion. The EDS spectrum and elemental mapping images for the standing MoO_2@C nanosheets on graphene are shown in Fig. 1f and S2 of ESI.† A few elements such as Mo, C, and O are observed, which were uniformly distributed within the composite.
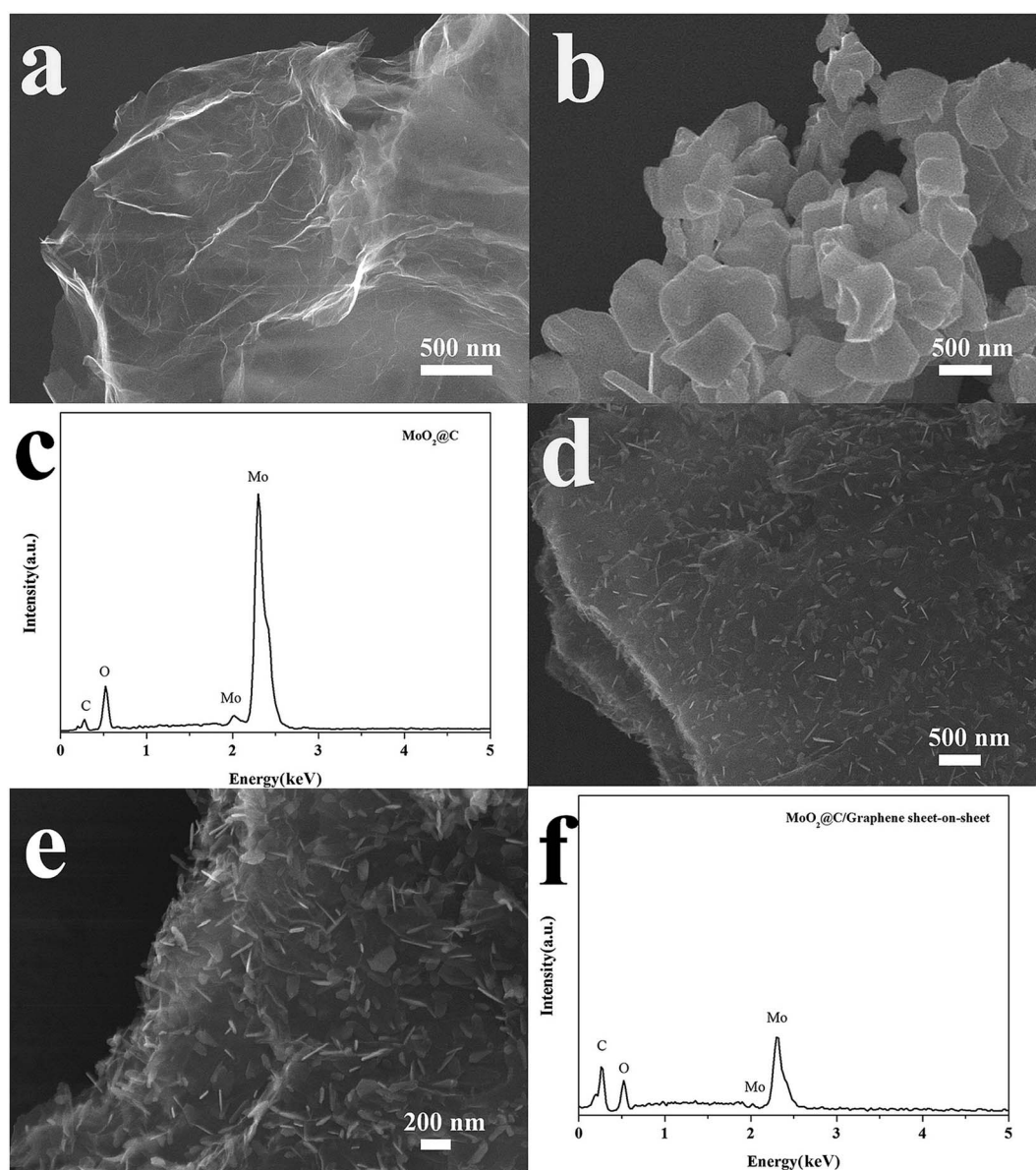

Fig. 1   SEM images of (a) graphene, (b) MoO_2@C, (c) the EDS spectrum of MoO_2@C, (d and e) the standing MoO_2@C nanosheets on graphene at low and high magnifications, (f) the EDS spectrum of the standing MoO_2@C nanosheets on graphene.

To further study the morphology and microstructure of the obtained products, TEM and HRTEM measurements were carried out. MoO_2@C sheets (~100–200 nm in size) were well wrapped by GNS (Fig. 2a–c), which can increase the electrical conductivity and mechanical stability of MoO_2 and on the other hand, the agglomeration of GNS can be prevented by the sandwiched MoO_2@C nanosheets. It is of interest to note that most sheet-like MoO_2@C structures stand on GNS with different angles toward graphene substrate, although several nanosheets remain flat on GNS surface. A number of black lines (for example, one indicated by a white rectangle) can be observed in Fig. 2b and c, which are the cross-section of standing MoO_2@C nanosheets under electron imaging because they are perpendicular to the graphene plane. Therefore, the thickness of MoO_2@C nanosheets can be indicated by the width of these observed lines to be ~20 nm. The stable standing nanosheets on GNS should be ascribed to the supporting effect of pyrolytic carbon around MoO_2, which is formed by acetylene decomposition. This carbon layer functions as cement to link graphene and the standing MoO_2 nanosheets and make the integrated 3D composite network stable. The crystalline structure of MoO_2 and ultra-thin carbon shell were further characterized by HRTEM. As shown in Fig. 2d, the lattice fringes of ~0.34 nm were observed, corresponding to the (110) plane of monoclinic MoO_2, moreover the disordered carbon structure of graphene and carbon shell around MoO_2 core can be also observed in this image; hence, lithium ions can still intercalate easily through the outer carbon shell or graphene wrapping. Fig. 2e shows the cross-section image of a standing MoO_2@C nanosheet chosen from Fig. 2c, which is perpendicular to the graphene plane. There is clearly a carbon shell (~6–8 nm) around MoO_2 in Fig. 2e. In comparison, a flat-lying MoO_2@C nanosheet chosen from Fig. 2c is shown in Fig. 2f. The thickness of carbon shell is estimated to be ~3 nm, which is substantially smaller than that of the standing product as shown in Fig. 2e. This should be ascribed to the different growth directions between the standing and flat-lying MoO_2@C nanosheets. The standing MoO_2 nanosheet has more contact/reaction area with the flowing acetylene gas in the preparation process compared to the flat-lying MoO_2 nanosheet, and therefore more acetylene may decompose around the erect nanosheet and form a thicker carbon layer. The HRTEM images provide direct evidence to confirm that most MoO_2 nanosheets grow erectly with the assistance of the carbon shell. If there is no carbon shell or the carbon shell is very thin, these nanosheets would tend to be flat on the graphene surface.

Flat-lying MoO_2 sheets were also obtained by a similar thermolysis of AHM in pure N_2 instead of a mixture of C_2H_2/N_2. Fig. 3a–c shows a MoO_2 sheets without a carbon shell. They have an average size of ~100–200 nm, which is similar to that of MoO_2@C sheets. These observed MoO_2 sheets lie flat on graphene and no nanosheet stands on the graphene surface. It is believed that the flat-lying nanosheet should be more stable than a standing nanosheet by large face-to-face contact with the graphene substrate because the thickness of the nanosheet is only ~20 nm, which is much smaller than the planar size of the
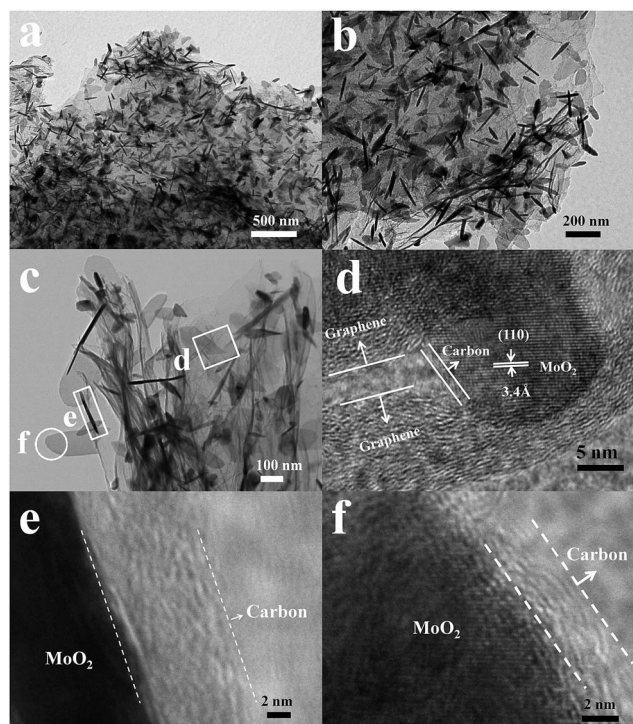

Fig. 2 TEM images of (a–c) the standing MoO_2@C nanosheets on graphene at different magnifications, HRTEM image of the standing MoO_2@C nanosheets on graphene showing (d) the MoO_2, carbon shell, and graphene, (e) a standing MoO_2@C core–shell nanosheet, (f) a flat-lying MoO_2@C core–shell nanosheet.
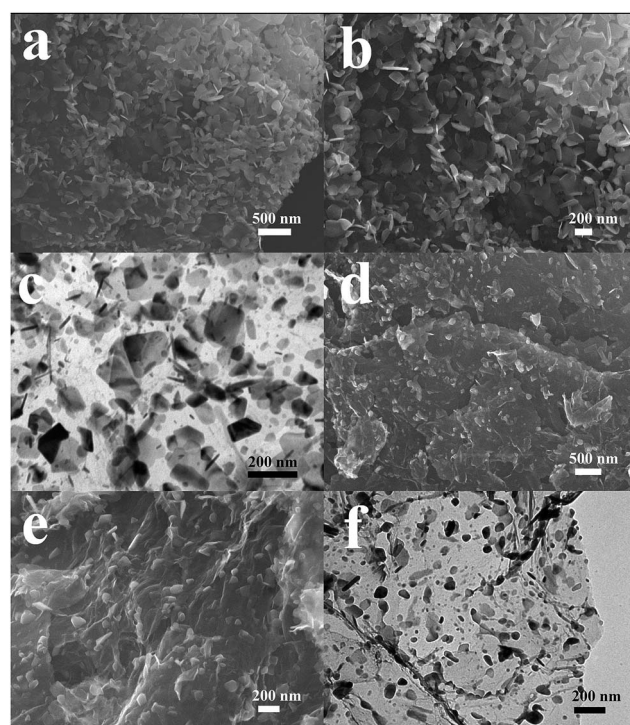

Fig. 3 The flat-lying MoO_2 nanosheets on graphene: (a and b) SEM images and (c) TEM image, the MoO_2/graphene particle-on-sheet composite: (d and e) SEM images and (f) TEM image.

This journal is © The Royal Society of Chemistry 2015

J. Mater. Chem. A, 2015, 3, 4706–4715 | 4709

sheet (~100–200 nm). Therefore this also confirms the supporting effect of pyrolytic carbon for stable standing $MoO_2@C$ nanosheets on graphene prepared in a C_2H_2-assisted thermolysis process. The nanosheets were unable to stand on graphene without the carbon support as shown clearly in Fig. 3c. Fig. 3d–f shows the product prepared in H_2 instead of C_2H_2. A large number of MoO_2 nanoparticles are observed on the GNS. These anchored MoO_2 particles are distributed uniformly with diameters of ~10–40 nm. Moreover, if PMA was used as the starting material instead of AHM, the morphology of MoO_2/graphene composite was largely different. A number of small MoO_2 nanorods with lengths of ~100–200 nm and diameters of ~10–20 nm are wrapped in the GNS layers (Fig. S3, ESI†). The TEM image in Fig. S3c† clearly shows the presence of many small MoO_2 nanoparticles (~5–10 nm) in the composite. Fig. S4 in the ESI† shows the effect of the reaction time on the final product. The morphologies of $MoO_2@C$ sheets are roughly unchanged, but $MoO_2@C$ nanosheets are not formed completely compared to the main product as shown in Fig. 2. These tattered nanosheets exhibit a smaller size of ~100–150 nm after a shorter reaction time. Based on the above discussion it can be noted that the experimental conditions, such as the gas atmosphere, the starting precursors, and reaction time, have important influences on the shape and size of the obtained MoO_2 crystals.

Fig. 4a shows the XRD patterns of various products, all the diffraction peaks of (110), (020), (220), (031), (−231) can be easily indexed to monoclinic MoO_2, which are in good agreement with the standard data (PDF 65-5787).[35] The sharp and intense peaks suggest the formation of highly crystalline MoO_2. For several MoO_2/C composites, the characteristic (002) peak for graphite is not evident, which should be ascribed to the low graphitic extent and the peak may be diminished by the strong (110) peak of MoO_2 at a similar position. Notably, MoO_3 are usually obtained by the decomposition of hexaammonium heptamolybdate (AHM) tetrahydrate in air; however, the presence of carbon or reducing gas can reduce MoO_3 to MoO_2.[36,37] The thermogravimetric analysis of MoO_2/graphene composites was carried out under an air atmosphere at a ramp rate of 10 °C min^{-1} (Fig. 4b). There is a small weight increase observed around 350–400 °C. This is mainly due to the oxidation of MoO_2 to MoO_3, which gains a theoretical weight increase of ~12.5 wt% (based on the mass of MoO_2). The decomposition of graphene occurs around 380–460 °C and the solid residue is MoO_3. The MoO_2 contents in the composites were be calculated to be 48.3%, 54.2% and 53.2% for the standing $MoO_2@C$ nanosheets on graphene, the flat-lying MoO_2 nanosheets on graphene and MoO_2/graphene particle-on-sheet composites, respectively. It is worth noting that the carbon content of the standing $MoO_2@C$ nanosheets on graphene is larger than the other two composites, which is ascribed to the formation of pyrolytic carbon in the standing $MoO_2@C$ nanosheets on graphene. This extra amount of pyrolytic carbon coating can be estimated to be around 5.4% in the composite based on the increased amount of carbon (pyrolytic carbon and graphene) in $MoO_2@C$/graphene compared to the average graphene amount in MoO_2/graphene sheet-on-sheet and particle-on-sheet composites. Raman spectrum in Fig. 4c displays both D-band at ~1320 cm^{-1}

and G-band at ~1590 cm^{-1} for graphene and MoO_2/graphene composites, respectively. The D/G intensity ratios of the standing $MoO_2@C$ nanosheets on graphene, the flat-lying MoO_2 nanosheets on graphene and MoO_2/Graphene particle-on-sheet are calculated to be 1.35, 1.33 and 1.31, respectively, which are all larger than bare graphene (1.18). It is indicated that hybridizing MoO_2 with graphene increases the content of disordered domains of graphene, which is caused by partially embedding of MoO_2 into the graphene layer. These generated defects may be beneficial to the electrolyte infusion and lithium ion storage. Nitrogen adsorption–desorption isotherms of three MoO_2/graphene composites are shown in Fig. 4d–f. Calculations based on isotherms show surface areas of 73.2, 132.2, and 136.2 m^2 g^{-1} for the standing $MoO_2@C$ nanosheets on graphene, the flat-lying MoO_2 nanosheets on graphene and MoO_2/graphene particle-on-sheet composites, respectively. These composites display similar sharp ~3.2–3.8 nm mesopore peaks, according to the inset pore size distribution curves. The smallest BET surface area of the standing $MoO_2@C$ nanosheets on graphene reveals that a layer of pyrolytic carbon may be also present on the graphene surface and therefore some micro/meso-pores are closed by the carbon coating/coverage. Notably, lithium ions can still diffuse into these closed pores through the formed disordered carbon layer (as shown in the HRTEM images of Fig. 2e and f); therefore, lithium-storage capacity is not reduced.

The CV curves of three MoO_2/graphene composites at a scan rate of 0.1 mV s^{-1} are presented in Fig. 5a. For the standing $MoO_2@C$ nanosheets on graphene, two pronounced redox couples are observed at 1.49/1.78 V and 1.12/1.48 V, which corresponds to a reversible phase transition (reversible change between the orthorhombic and the monoclinic phase) of the partially lithiated Li_xMoO_2.[13,14,16,49] There is a broad peak at ~0.63 V, corresponding to the reduction of electrolyte and formation a solid electrolyte interface (SEI) film on the surface of the anode. The flat-lying MoO_2 nanosheets on graphene and MoO_2/graphene particle-on-sheet composites exhibit similar redox peaks in the CV curves with increased voltage positions. Two redox peak pairs at 1.46/1.74 V, 1.25/1.55 V and 1.45/1.72 V, 1.27/1.56 V can be identified for the flat-lying MoO_2 nanosheets on graphene and MoO_2/graphene particle-on-sheet, respectively.

The first-cycle galvanostatic discharge (lithium insertion) and charge (lithium extraction) curves of graphene, $MoO_2@C$ (93.6% MoO_2), MoO_2/graphene particle-on-sheet composite (53.2% MoO_2), flat-lying MoO_2 nanosheets on graphene (54.2% MoO_2), and standing $MoO_2@C$ nanosheets on graphene (48.3% MoO_2, 5.4% carbon coating, and 46.3% graphene) are shown in Fig. 5b. The standing $MoO_2@C$ nanosheets on graphene exhibit initial discharge and charge capacities of 1255 mA h g^{-1} and 758 mA h g^{-1}, respectively, with a coulombic efficiency of 60.4%. The irreversible capacity loss in the first cycle arises from the irreversible lithium consumption and the formation of a solid electrolyte interface (SEI film) on the electrode surface. Two couples of plateaus are clearly observed that are in good agreement with the CV results. In comparison, the initial discharge and charge capacities were 626 and 1102 mA h g^{-1} for
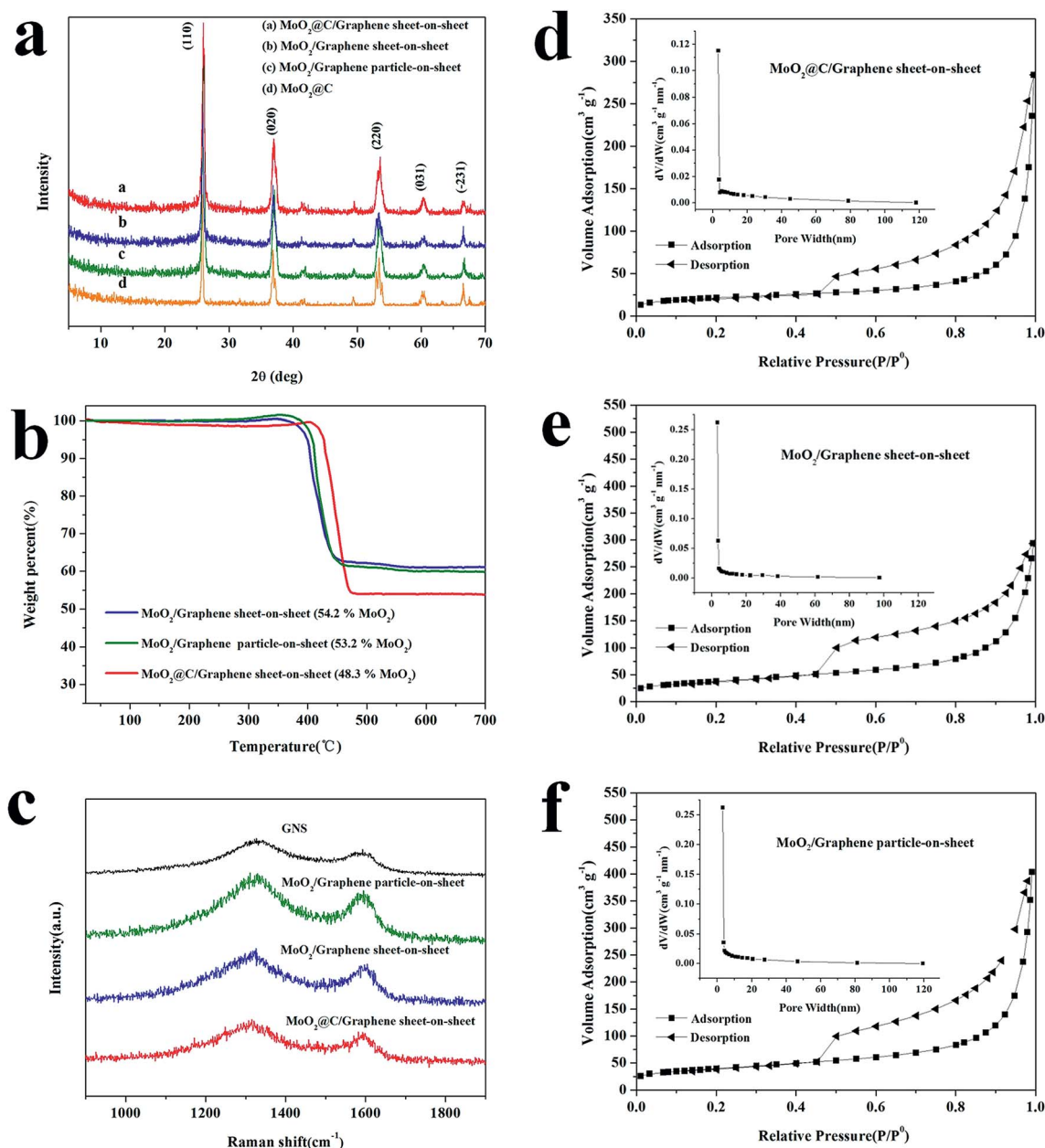
4710 | J. Mater. Chem. A, 2015, 3, 4706–4715

This journal is © The Royal Society of Chemistry 2015

Fig. 4 Various MoO_2-based composites: (a) XRD patterns, (b) TGA curves, (c) Raman spectra. Nitrogen adsorption–desorption isotherms: (d) the standing MoO_2@C nanosheets on graphene, (e) the flat-lying MoO_2 nanosheets on graphene, (f) the MoO_2/graphene particle-on-sheet composite.

the flat-lying MoO_2 nanosheets on graphene and 602 and 1095 mA h g^{-1} for the MoO_2/graphene particle-on-sheet composite. The first discharge and charge capacities of MoO_2@C were 263 and 370 mA h g^{-1}, respectively.

Fig. 5c shows the cycling performances of various products at a current density of 100 mA g^{-1}. The MoO_2@C product showed a small reversible capacity of 161 mA h g^{-1} after 100 cycles. GNS had a slightly larger reversible capacity of 276 mA h g^{-1} after 100 cycles. In the presence of graphene, the cycling performances were substantially improved for graphene/MoO_2 composites. The drastic volume change of MoO_2 during the cycling process can be buffered by graphene and the restacking of graphene

into graphite platelet can be prevented. The anode of the standing MoO_2@C nanosheets on graphene composite showed a large reversible capacity of 752 mA h g^{-1} after 100 cycles with a capacity retention rate of 99.2% compared to the first-cycle value. An average capacity fading of 0.008% per cycle can be calculated, indicating the excellent cycliability for the composite. Compared to the standing MoO_2@C nanosheets on graphene composite, the other two composites showed reduced reversible capacities. The flat-lying MoO_2 nanosheets on graphene composite had a capacity fading from 626 mA h g^{-1} to 472 mA h g^{-1} during 100 cycles. The MoO_2/graphene particle-on-sheet composite had the worst cycling performance among
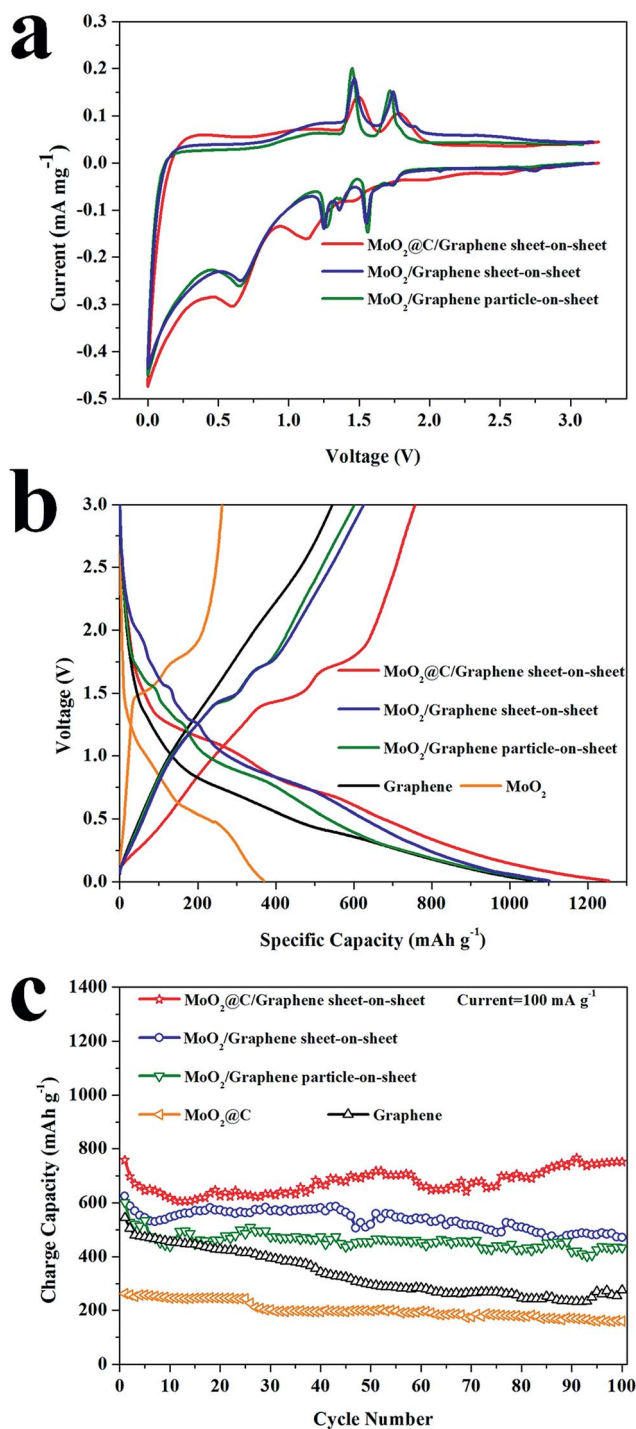
Fig. 5 Electrochemical performances of various MoO₂/graphene composites: (a) CV curves, (b) the first-cycle discharge (lithium insertion) and charge (lithium extraction) curves, (c) cycling performance at a current density of 100 mA g⁻¹ (0.1 C).
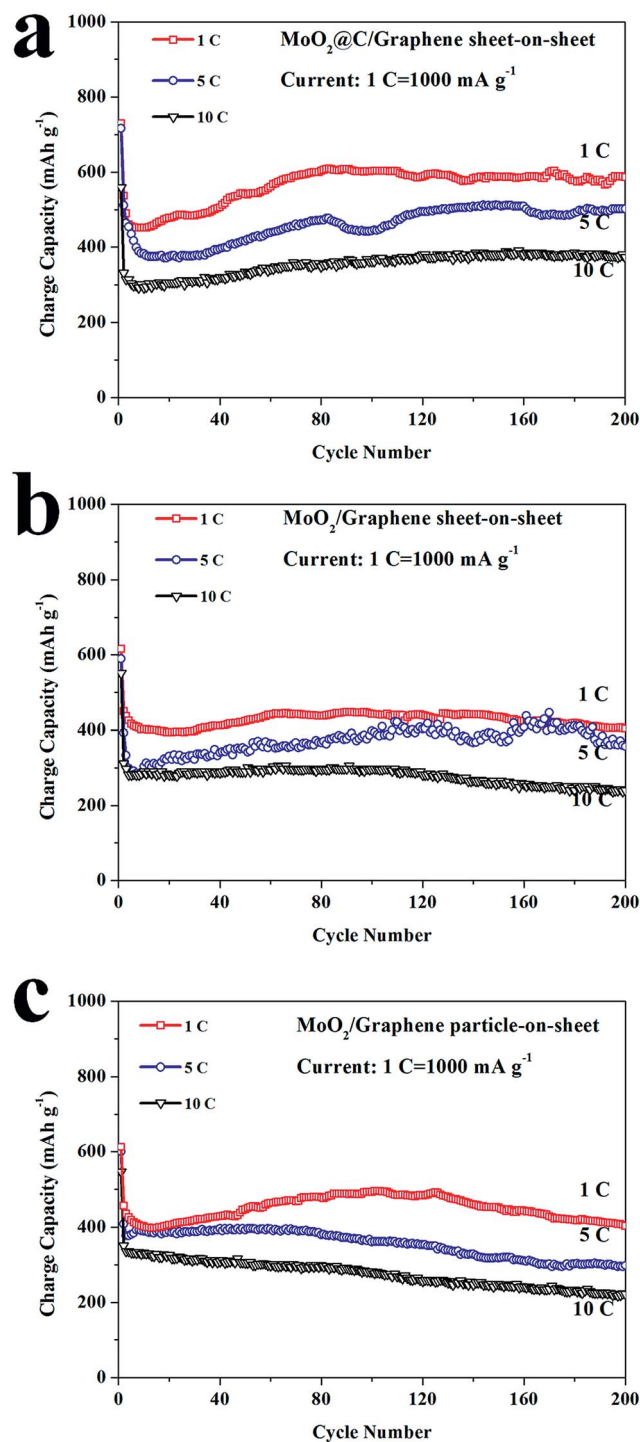

Fig. 6 High-rate cycling performances of (a) the standing MoO_2@C nanosheets on graphene, (b) the flat-lying MoO_2 nanosheets on graphene, (c) the MoO_2/graphene particle-on-sheet composite.

the three types of MoO_2/graphene composites because a small reversible capacity of 433 mA h g⁻¹ is retained after 100 cycles, corresponding to 71.9% of the initial value.

The high-rate cycling performances of the three types of MoO_2/graphene composites are compared in Fig. 6 and S5 of the ESI.† Large current rates of 1, 5, 10 C (1 C = 1000 mA h g⁻¹) were

used to measure their high-rate performances. In general, there was a fast capacity fading in the first five cycles for the three composites. The observed capacities tended to increase slightly during 10–80 cycles and were quite stable during the following cycles (~80–200 cycles). The slightly-increased reversible capacity during long cycling is also observed in the aforementioned Fig. 5c and in the previous reports.[24,33,39,40] This phenomenon has been

ascribed to the gradual activation process of the conversion reaction between MoO_2 and Mo as well as the improved Li-diffusion kinetics due to the partial crystallinity degradation of the electrode to a more disordered electrode structure.[33,40] The standing MoO_2@C nanosheets on graphene composite exhibited high initial charge capacities of 730, 717, 560 mA h g^{-1} at 1, 5, and 10 C, which are superior than those of the flat-lying MoO_2 nanosheets on graphene (616, 590, 551 mA h g^{-1}), MoO_2/graphene particle-on-sheet (613, 601, 547 mA h g^{-1}) and bare graphene (657, 362, 272 mA h g^{-1} as shown in Fig. S6 of ESI†). Highly reversible Li-ion storage capacities could be observed after repetitive cycling of the MoO_2@C/graphene sheet-on-sheet composite. For example, 587 and 502 mA h g^{-1} can be retained for the composite at 1 C and 5 C, respectively, after 200 cycles. In comparison, the flat-lying MoO_2 nanosheets on graphene exhibited smaller reversible capacities than the standing MoO_2@C nanosheets on graphene composite at high current rates, and their high-rate cycling performances were better than the MoO_2/graphene particle-on-sheet composite. The smallest reversible capacities of 403, 298, and 222 mA h g^{-1} after 200 cycles were observed for the MoO_2/graphene particle-on-sheet composite at current rates of 1, 5, and 10 C, respectively. To the best of our knowledge, the observed excellent high-rate performance (above 500 mA h g^{-1} during 200 cycles at 5 A g^{-1}) for the standing MoO_2@C nanosheets on graphene has not been witnessed previously in various MoO_2-based anodes.[4–40]

The electrochemical impedance spectra of MoO_2/graphene composites over the frequency range were carried out to investigate the electrode kinetics (Fig. S7†). The semicircles in the medium frequency are believed to reflect the charge-transfer resistance (R_{ct}). Based on the equivalent circuit, the charge-transfer resistance (R_{ct}) of the carbon-coated MoO_2 particle was determined to be 98.5 Ω, which is decreased to 84.5 Ω for graphene supported MoO_2 nanoparticles. The value of R_{ct} is further decreased to 77.3 Ω for the flat-lying MoO_2 nanosheets on graphene, which is possibly due to the larger contact area between MoO_2 nanosheets and GNS compared to that of the particle-on-sheet composite. The standing MoO_2@C nanosheets on graphene composite exhibits the smallest diameter in the semi-circle and a small resistance of 23.0 Ω was be determined. The fastest charge-transfer could be due to the multiple synergetic effects in the composite, including a sheet-like MoO_2 structure, graphene support, carbon coating, and integrated 3D porous structure, associated with the standing MoO_2 nanosheets on graphene.

The effect of weight ratio of MoO_2 to graphene is explored for optimizing the electrochemical performance of the standing MoO_2 nanosheets on graphene. Fig. 7a and b and S8 of the ESI† show SEM images of the standing MoO_2 nanosheets on graphene composites with various loading amounts of MoO_2. It is clear that a suitable weight ratio of MoO_2 to graphene is crucial for the composite morphology. MoO_2 nanosheets can be
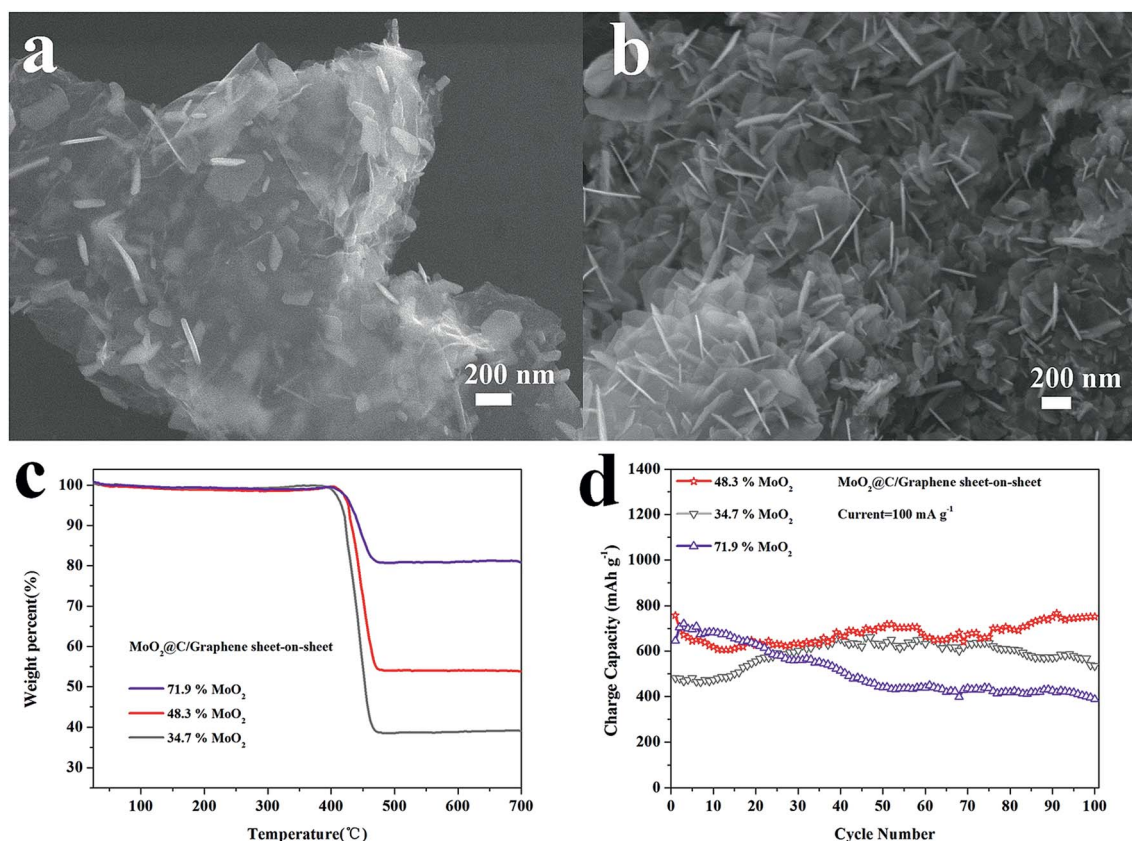

Fig. 7 The MoO_2@C nanosheets on graphene with different amounts of MoO_2: (a) SEM image of the composite with 34.7% MoO_2, (b) SEM image of the composite with 71.9% MoO_2, (c) TGA curves, (d) cycling performance at a current density of 100 mA g^{-1} (0.1 C).

This journal is © The Royal Society of Chemistry 2015

J. Mater. Chem. A, 2015, 3, 4706–4715 | 4713

observed (Fig. 7a and b and S8a–d†) in the range of MoO_2 loading from 34.7% to 71.9% (as calculated by TGA analysis in Fig. 7c) and higher loading would lead to a heavy agglomeration of MoO_2 materials without the sheet-like morphology on graphene (Fig. S8e and f†). Fig. 7d and S9 of the ESI† shows a comparison of the electrochemical performances of the MoO_2@C/graphene composites with different loading amounts of MoO_2. The initial charge/discharge capacities were 646/1219 and 482/909 mA h g^{-1} for MoO_2@C/graphene (34.7% MoO_2) and MoO_2@C/graphene (71.9% MoO_2) composites, respectively (Fig. S9†). The corresponding charge capacities were retained at 388 and 535 mA h g^{-1} after 100 cycles for the two composites (Fig. 7d). Therefore, these results demonstrate that the main product of MoO_2@C/graphene (48.3% MoO_2) exhibits the best performance (752 mA h g^{-1} after 100 cycles) compared with the other two composites with higher or lower loading of MoO_2. It is suggested that the optimal value for MoO_2 loading must be between 34.7% and 71.9% and may be close to the value of the main product of this work (48.3%). It is because the weight ratios of MoO_2 to GNS have important influences on the morphology, size and distribution of MoO_2 on GNS. In the presence of a large amount of GNS, the restacking of graphene may still take place because there are not sufficient "spacer" materials (MoO_2 nanosheets). On the contrary, in the presence of a small amount of GNS, MoO_2 materials are too crowded on the GNS surface, in which the volume variation cannot be buffered efficiently by GNS. Fig. S8e and f of the ESI† shows the MoO_2@C/graphene composites with a high loading of MoO_2 (85.7% and 95.2% MoO_2). The obtained MoO_2 in Fig. S8f† is similar to that of MoO_2@C in the absence of GNS and no sheet-like morphology can be observed.

The excellent cycling performances of the standing MoO_2 nanosheets on graphene composite should be ascribed to the 3D porous hierarchical nanostructure. Carbon coating and graphene support both have beneficial effects for enhanced electrochemical properties, which have been explored extensively in previous studies.[20–28,33–40] The increased electrical contact, the improved mechanical stability, and the facilitated lithium diffusion have usually been determined for carbon coatings[20–28] and graphene supports.[33–40] Besides these effects, it is emphasized here that carbon coating can help MoO_2 achieve a novel standing orientation on a GNS surface. The resultant 3D porous hierarchical network in the electrode can exhibit more open and porous space, and therefore facilitate the charge transfer and electrolyte infusion. These void spaces among erect MoO_2 nanosheets are also useful to accommodate the large volume expansion during cycling. Moreover, the erect MoO_2 nanosheets have two-sides of the exposed faces for lithium insertion and extraction. The restacking of graphene is more efficiently prevented by the erect MoO_2 nanosheets between two neighboring graphene nanosheets in this 3D porous hierarchical nanostructure. The cycled composite electrode was examined again by XRD patterns (Fig. S10a†) and TEM image (Fig. S10b†). The initial crystalline MoO_2 structure was changed to amorphous after 100 cycles and the standing sheet structure can be still observed despite the presence of PVDF binder and carbon black.

Conclusion

In summary, this work reports several MoO_2/graphene morphologies: graphene supported MoO_2 nanoparticles, MoO_2 nanorods, and two unprecedented MoO_2 nanostructures (MoO_2 nanosheets and standing MoO_2@C core–shell nanosheets on graphene) by adjusting the experimental conditions of a facile one-pot thermolysis synthesis approach. The growth mechanism of various MoO_2-based nanostructures and their morphology-dependent Li-ion storage properties are also explored. Excellent cycling performances at both small and high current densities are achieved for the standing MoO_2 nanosheets on a graphene composite. Large reversible capacities of more than 500 mA h g^{-1} can be delivered during 200 discharge/charge cycles at an extremely large current of 5 A g^{-1}.

Acknowledgements

References

1 A. Manthiram and J. Phys, *Chem. Lett.*, 2011, **2**, 176.

2 Z. Y. Zhou, N. Tian, J. T. Li, I. Broadwell and S. G. Sun, *Chem. Soc. Rev.*, 2011, **40**, 4167.

3 C. M. Sim, Y. J. Hong and Y. C. Kang, *ChemSusChem*, 2013, **6**, 1320.

4 Y. L. Liu, H. Zhang, P. Ouyang, W. H. Chen, Y. Wang and Z. C. Li, *J. Mater. Chem. A*, 2014, **2**, 4714.

5 Y. M. Sun, X. L. Hu, J. C. Yu, Q. Li, W. Luo, L. X. Yuan, W. X. Zhang and Y. H. Huang, *Energy Environ. Sci.*, 2011, **4**, 2870.

6 J. H. Ku, J. H. Ryu, S. H. Kim, O. H. Han and S. M. Oh, *Adv. Funct. Mater.*, 2012, **22**, 3658.

7 J. Liu, S. S. Tang, Y. K. Lu, G. M. Cai, S. Q. Liang, W. J. Wang and X. L. Chen, *Energy Environ. Sci.*, 2013, **6**, 2691.

8 Y. L. Liu, H. Zhang, P. Ouyang and Z. C. Li, *Electrochim. Acta*, 2013, **102**, 429.

9 J. H. Ku, Y. S. Jung, K. T. Lee, C. H. Kim and S. M. Oh, *J. Electrochem. Soc.*, 2009, **156**, A688.

10 L. C. Yang, Q. S. Gao, Y. H. Zhang, Y. Tang and Y. P. Wu, *Electrochem. Commun.*, 2008, **10**, 118.

11 D. Koziej, M. D. Rossell, B. Ludi, A. Hintennach, P. Novák, J. D. Grunwaldt and M. Niederberger, *Small*, 2011, 7, 377.

12 X. Zhang, X. Z. Zeng, M. Yang and Y. X. Qi, *Eur. J. Inorg. Chem.*, 2014, **2014**, 352.

13 B. K. Guo, X. P. Fang, B. Li, Y. F. Shi, C. Y. Ouyang, Y. S. Hu, Z. X. Wang, G. D. Stucky and L. Q. Chen, *Chem. Mater.*, 2012, **24**, 457.

14 H. J. Zhang, J. Shu, K. X. Wang, X. T. Chen, Y. M. Jiang, X. Wei and J. S. Chen, *J. Mater. Chem. A*, 2014, **2**, 80.

4714 | *J. Mater. Chem. A*, 2015, **3**, 4706–4715

This journal is © The Royal Society of Chemistry 2015

15 H. J. Zhang, K. X. Wang, X. Y. Wu, Y. M. Jiang, Y. B. Zhai, C. Wang, X. Wei and J. S. Chen, *Adv. Funct. Mater.*, 2014, **24**, 3399.

16 Y. F. Shi, B. K. Guo, S. A. Corr, Q. H. Shi, Y. S. Hu, K. R. Heier, L. Q. Chen, R. Seshadri and G. D. Stucky, *Nano Lett.*, 2009, **9**, 4215.

17 X. P. Fang, B. K. Guo, Y. F. Shi, B. Li, C. X. Hua, C. H. Yao, Y. C. Zhang, Y. S. Hu, Z. X. Wang, G. D. Stucky and L. Q. Chen, *Nanoscale*, 2012, **4**, 1541.

18 X. F. Zhang, X. X. Song, S. Gao, Y. M. Xu, X. L. Cheng, H. Zhao and L. H. Huo, *J. Mater. Chem. A*, 2013, **1**, 6858.

19 X. Y. Zhao, M. H. Cao, B. Liu, Y. Tian and C. W. Hu, *J. Mater. Chem.*, 2012, **22**, 13334.

20 B. Liu, X. Y. Zhao, Y. Tian, D. Zhao, C. W. Hu and M. H. Cao, *Phys. Chem. Chem. Phys.*, 2013, **15**, 8831.

21 Y. M. Sun, X. L. Hu, W. Luo and Y. H. Huang, *J. Mater. Chem.*, 2012, **22**, 425.

22 Z. Y. Wang, J. S. Chen, T. Zhu, S. Madhavi and X. W. Lou, *Chem. Commun.*, 2010, **46**, 6906.

23 L. Zhou, H. B. Wu, Z. Y. Wang and X. W. Lou, *ACS Appl. Mater. Interfaces*, 2011, **3**, 4853.

24 H. J. Zhang, T. H. Wu, K. X. Wang, X. Y. Wu, X. T. Chen, Y. M. Jiang, X. Wei and J. S. Chen, *J. Mater. Chem. A*, 2013, **1**, 12038.

25 S. Yoon and A. Manthiram, *J. Mater. Chem.*, 2011, **21**, 4082.

26 W. Luo, X. L. Hu, Y. M. Sun and Y. H. Huang, *Phys. Chem. Chem. Phys.*, 2011, **13**, 16735.

27 Q. S. Gao, L. C. Yang, X. C. Lu, J. J. Mao, Y. H. Zhang, Y. Q. Wu and Y. Tang, *J. Mater. Chem.*, 2010, **20**, 2807.

28 L. C. Yang, L. L. Liu, Y. S. Zhu, X. J. Wang and Y. P. Wu, *J. Mater. Chem.*, 2012, **22**, 13148.

29 A. L. Chen, C. X. Li, R. Tang, L. W. Yin and Y. X. Qi, *Phys. Chem. Chem. Phys.*, 2013, **15**, 13601.

30 L. X. Zeng, C. Zheng, C. L. Deng, X. K. Ding and M. D. Wei, *ACS Appl. Mater. Interfaces*, 2013, **5**, 2182.

31 A. Bhaskar, M. Deepa and T. N. Rao, *ACS Appl. Mater. Interfaces*, 2013, **5**, 2555.

32 J. P. Jegal, H. K. Kim, J. S. Kim and K. B. Kim, *J. Electroceram.*, 2013, **31**, 218.

33 A. Bhaskar, M. Deepa, T. N. Rao and U. V. Varadaraju, *J. Power Sources*, 2012, **216**, 169.

34 K. H. Seng, G. D. Du, L. Li, Z. X. Chen, H. K. Liu and Z. P. Guo, *J. Mater. Chem.*, 2012, **22**, 16072.

35 P. X. Han, W. Ma, S. P. Pang, Q. S. Kong, J. H. Yao, C. F. Bi and G. L. Cui, *J. Mater. Chem. A*, 2013, **1**, 5949.

36 Y. J. Chen, X. P. Di, C. Ma, C. L. Zhu, P. Gao, J. Q. Li, C. W. Sun and Q. Y. Ouyang, *RSC Adv.*, 2013, **3**, 17659.

37 Y. Xu, R. Yi, B. Yuan, X. F. Wu, M. Dunwell, Q. L. Lin, L. Fei, S. G. Deng, P. Andersen, D. H. Wang and H. M. Luo, *J. Phys. Chem. Lett.*, 2012, **3**, 309.

38 F. F. Xia, X. L. Hu, Y. M. Sun, W. Luo and Y. H. Huang, *Nanoscale*, 2012, **4**, 4707.

39 Q. W. Tang, Z. Q. Shan, L. Wang and X. Qin, *Electrochim. Acta*, 2012, **79**, 148.

40 Y. M. Sun, X. L. Hu, W. Luo and Y. H. Huang, *ACS Nano*, 2011, **5**, 7100.

41 P. Chen, F. D. Wu and Y. Wang, *ChemSusChem*, 2014, **7**, 1407.

42 Y. Gu, F. D. Wu and Y. Wang, *Adv. Funct. Mater.*, 2013, **23**, 893.

43 Y. Gu and Y. Wang, *RSC Adv.*, 2014, **4**, 8582.

44 J. Kan and Y. Wang, *Sci. Rep.*, 2013, **3**, 3502.

45 P. Chen, Y. Su, H. Liu and Y. Wang, *ACS Appl. Mater. Interfaces*, 2013, **5**, 12073.

46 L. Q. Lu, L. J. Lu and Y. Wang, *J. Mater. Chem. A*, 2013, **1**, 9173.

47 Y. Gu, Y. Xu and Y. Wang, *ACS Appl. Mater. Interfaces*, 2013, **5**, 801.

48 P. Chen, L. Guo and Y. Wang, *J. Power Sources*, 2013, **222**, 526.

49 J. R. Dahn and W. R. McKinnon, *Solid State Ionics*, 1987, **23**, 1.